Chiral anomaly of Weyl magnons in stacked honeycomb ferromagnets

Ying Su and X. R. Wang*

Physics Department, The Hong Kong University of Science and Technology, Clear Water Bay, Kowloon, Hong Kong and HKUST Shenzhen Research Institute, Shenzhen 518057, China

(Received 6 March 2017; published 26 September 2017)

One of the most important signatures of Weyl materials is the chiral anomaly. So far, there has been little study of chiral anomaly of Weyl magnons, featured by nontrivial band crossings at paired Weyl nodes of opposite chirality, while the anomaly for its electronic counterpart can routinely be observed in experiments. Here a road map for realizing and detecting the chiral anomaly of Weyl magnons in stacked honeycomb ferromagnets that are shown to be a Weyl magnetic material is provided. Using the Aharonov-Casher effect that is about the interaction between magnetic moments and electric fields, the magnon motion in honeycomb ferromagnetic layers can be quantized into magnonic Landau levels by a proper inhomogeneous electric field. The zeroth magnonic Landau level is chiral so that, under a magnetic field gradient, Weyl magnons propagate unidirectionally from one Weyl node to the other and reverse their chiralities, resulting in the magnonic chiral anomaly. A net magnon current carrying spin and heat through the zeroth magnonic Landau level depends linearly on the magnetic field gradient and the electric field gradient in the linear transport region. The linear spin and heat conductance can serve as the signatures of magnonic chiral anomaly. Furthermore, an experimental realization is proposed.

DOI: 10.1103/PhysRevB.96.104437

I. INTRODUCTION

Topological magnetic states have attracted enormous attention in recent years [1–23], because of their fundamental involvement and importance in magnonics, which is about the generation, detection, and manipulation of magnons and magnon current [24–27]. Magnons, the quanta of low-energy excitations of magnetic materials, can carry, process, and transmit information [28,29] like electrons besides being a control knob of magnetization dynamics [30–32]. So far, almost all studies on Weyl magnons (WMs) focus on the nontrivial band topology of Weyl nodes (WNs) and magnonic surface states in pyrochlore magnetic materials [19–21]. There has been little study of the magnonic chiral anomaly (MCA) because of its intrinsic difficulties. The realization and detection of the MCA is the main theme of this work.

In order to realize the MCA, one needs three-dimensional Weyl magnetic materials and a way to quantize magnon motion into magnonic Landau levels (MLLs) so that the zeroth MLL connecting two paired WNs exists. Then WMs can be pumped from one WN to the other through the zeroth MLLs under driving forces, resulting in the MCA. Because magnons are charge neutral particles and magnonic WNs appear usually at high energy [19–21], it is nontrivial to realize MLLs, as well as to inject magnons into the high-energy WNs. In this paper, we provide a road map for realizing the MCA. We show that stacked honeycomb ferromagnets can be a Weyl magnetic material of both type-I and type-II WMs with either one pair or two pairs of WNs. Magnons can interact with electric fields through the Aharonov-Casher (AC) effect [33] that can quantize the magnon motion into MLLs by using a proper inhomogeneous electric field. A net magnon current carrying spin and heat through the zeroth magnonic Landau level depends linearly on the magnetic field gradient and the electric field gradient in the linear transport region. The linear spin and heat conductance can serve as the signatures of the MCA. Furthermore, an experimental realization is proposed.

II. MODEL: STACKED HONEYCOMB FERROMAGNETS

We consider stacked honeycomb ferromagnets as shown in Fig. 1(a). The honeycomb lattices (in the xy plane) are aligned in the z direction. The in-plane vectors $\boldsymbol{a}_\alpha$ (red arrows) and $\boldsymbol{b}_\alpha$ (green arrows) ($\alpha = 1,2,3$) defined in honeycomb layers connect the nearest-neighbor (NN) and next-nearest-neighbor (NNN) lattice sites [34], respectively. A and B denote two sublattices of honeycomb layers. The layer separation is the same as the distance between two NN intralayer lattice sites that is set as unity. The spin Hamiltonian of a stacked honeycomb ferromagnet reads

$$H = -J\sum_{\langle i,j\rangle,l}\boldsymbol{S}_{i,l}\cdot\boldsymbol{S}_{j,l} - \sum_{i,l}K_i S_{i,l}^{z2} - \sum_{i,\langle l,l'\rangle}J_i\boldsymbol{S}_{i,l}\cdot\boldsymbol{S}_{i,l'} + D\sum_{\langle\langle i,j\rangle\rangle,l}\nu_{ij}\hat{\boldsymbol{z}}\cdot(\boldsymbol{S}_{i,l}\times\boldsymbol{S}_{j,l}) - g\mu_B B_0\sum_{i,l}S_{i,l}^{z}, \quad (1)$$

where i and j label lattice sites of honeycomb layers, and l and l' are layer indexes. $\langle i,j\rangle$ and $\langle\langle i,j\rangle\rangle$ denote the NN and NNN intralayer lattice sites, and $\langle l,l'\rangle$ are the NN layers. $\boldsymbol{S}_{i,l}$ is the spin (in units of $\hbar$) at site i of layer l. The first term describes the NN intralayer ferromagnetic exchange interaction with $J > 0$. The second term is the anisotropy energy with easy axis along the z direction and the third term is the NN interlayer exchange interaction. Here $K_i = K_{\rm A}$ ($K_{\rm B}$) and $J_i = J_{\rm A}$ ($J_{\rm B}$) for sites on sublattice A (B). The fourth term is the Dzyaloshinskii-Moriya interaction [17,35] and $\nu_{ij} = (2/\sqrt{3})(\hat{\boldsymbol{d}}_1\times\hat{\boldsymbol{d}}_2)_z = \pm 1$, where $\hat{\boldsymbol{d}}_1$ and $\hat{\boldsymbol{d}}_2$ are the unit vectors along NN intralayer bonds connecting the common NN site of i and j to sites j and i. The last term is the Zeeman interaction due to the external magnetic field B_0 along the z direction ($B_0 = 0$ is assumed below since it only shifts the energy). The ubiquitous magnetic dipole-dipole interaction is omitted since it is much weaker than other

*Corresponding author: phxwan@ust.hk

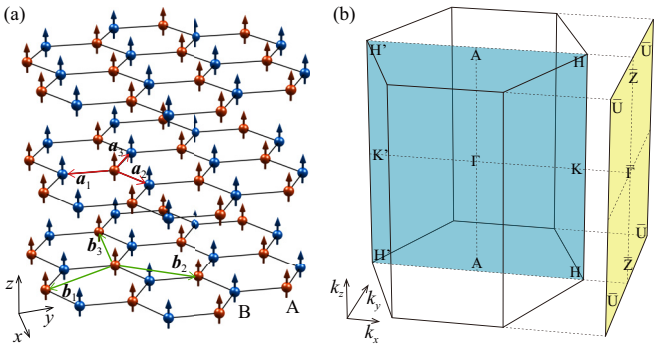

FIG. 1. (a) Schematic diagram of stacked honeycomb ferromagnets. Each site has a spin polarized in the z direction, represented by a red dot with an arrow on sublattice A and a blue dot with an arrow on sublattice B. (b) The first bulk Brillouin zone (BZ) and the first (100) surface BZ of stacked honeycomb ferromagnets.

interactions and the physics is unaffected (see Appendixes A and B).

III. PHASE DIAGRAM

Under the Holstein-Primakoff transformation [36], spin Hamiltonian Eq. (1) is mapped to a magnon Hamiltonian (see Appendix A) whose phase diagram is shown in Fig. 2 in which $K_\pm = K_A \pm K_B$ and $J_\pm = J_A \pm J_B$. Five distinct phases (colored differently) exist. Two magnon bands of Hamiltonian Eq. (A2) are gapped in both green and white regions. The green region is a topologically nontrivial phase in which topologically protected surface states exist in the bulk band gap (see Appendixes C and D) and this phase is called the topological magnon insulator in the literature [5]. On the other hand, the white regions are topologically trivial phases. The rest of the regions in Fig. 2 belong to three different WM phases: (i) WMs in the pink regions have one pair of WNs at $\boldsymbol{k}_1^\pm = (-4\pi/3\sqrt{3},0,\pm\cos^{-1} f_1)$, (ii) WMs in the yellow regions have one pair of WNs at $\boldsymbol{k}_2^\pm = (4\pi/3\sqrt{3},0,\pm\cos^{-1} f_2)$, (iii) WMs in the purple regions have two pairs of WNs at $\boldsymbol{k}_1^\pm$ and $\boldsymbol{k}_2^\pm$ simultaneously. Here $f_\eta = K_-/J_- + 1 + (-1)^\eta 3\sqrt{3}D/J_-$ for $\eta = 1$ or 2.

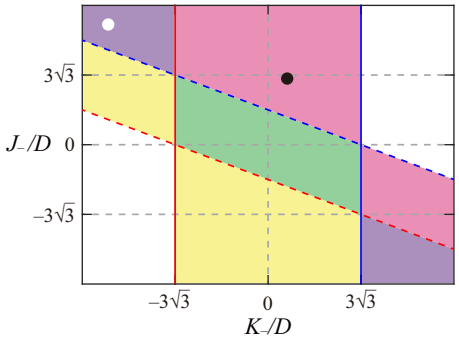

FIG. 2. Phase diagram of stacked honeycomb ferromagnets in the K_-/D-J_-/D plane. The yellow, pink, and purple regions denote three different WM phases. The green region is a topological magnon insulator phase, while the white regions are trivial phases.

In the WM phases, the effective Weyl Hamiltonian (to the first order in the momentum deviation $\boldsymbol{q} = \boldsymbol{k} - \boldsymbol{k}_\eta^\pm$) around the WN at $\boldsymbol{k}_\eta^\pm$ is

$$\mathcal{H}_\eta^\pm(\boldsymbol{q}) = (\varepsilon_\eta + \hbar u_{\eta,z}^\pm q_z)I + \sum_{\beta=x,y,z} \hbar v_{\eta,\beta}^\pm q_\beta \sigma_\beta, \qquad (2)$$

where $\varepsilon_\eta = 3JS + K_+S + J_+S(1 - f_\eta)$, $u_{\eta,z}^\pm = \pm J_+S\sqrt{1-f_\eta^2}/\hbar$, $v_{\eta,x}^\pm = (-1)^\eta 3JS/2\hbar$, $v_{\eta,y}^\pm = 3JS/2\hbar$, and $v_{\eta,z}^\pm = \pm J_-S\sqrt{1-f_\eta^2}/\hbar$. I, σ_x, σ_y, and σ_z are the 2×2 identity matrix and three Pauli matrices, respectively. The Berry curvature around the WN is $\boldsymbol{\Omega}(\boldsymbol{k}_\eta^\pm + \boldsymbol{q}) = (\prod_\beta v_{\eta,\beta}^\pm \boldsymbol{q})(\sum_\beta v_{\eta,\beta}^{\pm 2} q_\beta^2)^{-3/2}/2$ and the chirality of the WN is $C_\eta^\pm = \mathrm{sgn}(\prod_\beta v_{\eta,\beta}^\pm) = \pm(-1)^\eta \mathrm{sgn}(J_-)$. Thus, WNs are monopoles of Berry curvature and appear in pairs with opposite chirality as required by the no-go theorem [37–39]. According to the classification of Weyl semimetals [40,41], WMs are type-II when $|u_{\eta,z}^\pm| > |v_{\eta,z}^\pm| \Rightarrow |J_+| > |J_-|$ (see Appendix E), otherwise WMs are type-I. At the phase boundary crossing points $(K_-/D, J_-/D) = (\pm 3\sqrt{3},0)$, the system becomes nodal-line magnons in which two energy bands cross on H′K′H′ and HKH of the first bulk BZ as shown in Fig. 1(b), respectively (see Appendix F).

To visualize the WNs identified above, we fix the model parameters $D = 0.2J$, $K_+ = 12D$, $J_+ = 2D$, and $(K_-, J_-) = (D,5D)$ or $(-9D,9D)$ in the WM phases (marked by the black and white dots in Fig. 2). Energy bands in the k_x-k_z plane for fixed $k_y = 0$ [the blue plane in Fig. 1(b)] of the WMs are shown in Figs. 3(a) and 3(b) in which one and two pairs of WNs appear. The red and blue dots denote chirality ± 1 of the WNs. The corresponding Berry curvatures are as shown in Figs. 3(c) and 3(d), respectively, in which the black arrows encode the direction of Berry curvatures projected onto the k_x-k_z plane and the background color represents the divergence of Berry curvature $\nabla_{\boldsymbol{k}} \cdot \boldsymbol{\Omega}(\boldsymbol{k})$ with red for positive and blue for negative. Thus, the red and blue spots in Figs. 3(c) and 3(d) are indeed monopoles of Berry curvature and correspond to the WNs in Figs. 3(a) and 3(b). The spectral functions on the front (100) surface along $\bar{Z}\bar{\Gamma}\bar{Z}$ of the first (100) surface BZ [see Fig. 1(b)] are shown in Figs. 3(e) and 3(f), respectively. The surface states with high density (red color) on the front surface between WNs can be clearly seen. Near the energy of WNs, these surface states form magnon arcs (an analog of the Fermi arcs) on sample surfaces (see Appendix G).

IV. MAGNONIC LANDAU LEVEL

According to the AC effect [33], a magnon with the magnetic moment $\boldsymbol{\mu} = g\mu_B\hat{\boldsymbol{z}}$ interacts with an electric field $\boldsymbol{E}$ and acquires the AC phase, $\phi_{ij} = (1/\hbar c^2)\int_j^i (\boldsymbol{E}\times\boldsymbol{\mu})\cdot d\boldsymbol{r}$. This effect is reminiscent of the magnetic field effect on electrons and $\nabla\times(\boldsymbol{E}\times\boldsymbol{\mu})$ plays the role of the magnetic field so that the MLLs arise according to the theoretical proposal in Ref. [42]. Here we consider WMs under an inhomogeneous electric field $\boldsymbol{E} = (\mathcal{E}x,0,0)$. Compare the AC phase $\phi_{ij} = (g\mu_B/\hbar c^2)\int_i^j \mathcal{E}x dy$ for magnons with the Aharonov-Bohm phase for electrons; the lattice momentum in the effective Weyl Hamiltonian Eq. (2) should be replaced by $-i\hbar\nabla + g\mu_B\mathcal{E}x\hat{\boldsymbol{y}}/c^2$. The effective Weyl Hamiltonian

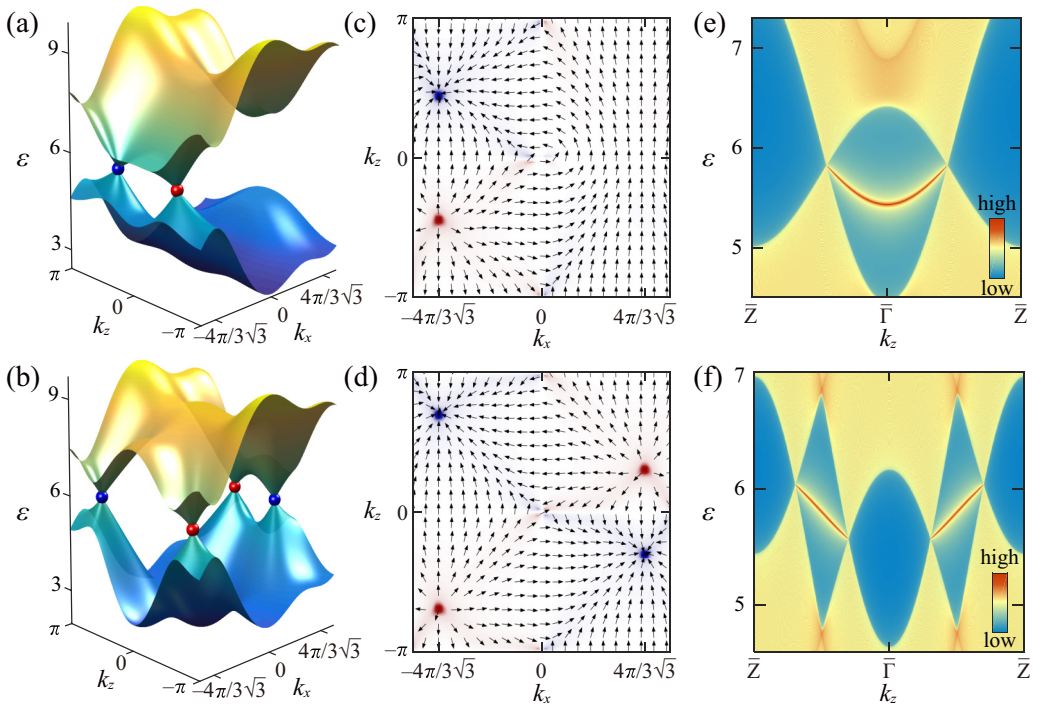

FIG. 3. (a) and (b) Band structures of WMs marked by the black and white dots in Fig. 2, respectively. The WNs of chirality ± 1 are marked by red and blue dots. (c) and (d) Corresponding Berry curvatures of the lower magnon bands in panels (a) and (b). The arrows represent the direction of Berry curvature vectors in the k_x-k_z plane with $k_y = 0$. The background color denotes the divergence of Berry curvature, where red and blue represent positive and negative values. (e) and (f) Density plots of the front (100) surface spectral functions along $\bar{Z}\bar{\Gamma}\bar{Z}$ for the energy bands in panels (a) and (b). Energy ε is in units of JS, and insets are color bars.

in the electric field can be solved exactly and the magnon motion in the x-y plane is quantized into MLLs with the eigenvalues

$$\begin{aligned}\varepsilon^{\pm}_{\eta,n\geqslant 1}(q_z) &= \varepsilon_\eta + \hbar u^{\pm}_{\eta,z} q_z \pm \hbar\sqrt{\lambda_\eta n + v^{\pm 2}_{\eta,z} q_z^2},\\ \varepsilon^{\pm}_{\eta,0}(q_z) &= \varepsilon_\eta + \hbar u^{\pm}_{\eta,z} q_z - (-1)^\eta \mathrm{sgn}(\mathcal{E})\hbar v^{\pm}_{\eta,z} q_z,\end{aligned} \tag{3}$$

where $\lambda_\eta = 2|v^{\pm}_{\eta,x} v^{\pm}_{\eta,y}|/l_{\mathcal{E}}^2$ and the electric length $l_{\mathcal{E}} = \sqrt{\hbar c^2/g\mu_B|\mathcal{E}|}$ is an analog of the magnetic length for electrons [42]. The MLL degeneracy is $D = L_x L_y/2\pi l_{\mathcal{E}}^2 \propto |\mathcal{E}|$, where L_x and L_y are the sample lengths in the x and y directions. The zeroth MLL $\varepsilon^{\pm}_{\eta,0}(q_z)$ is chiral and linearly dispersed with opposite group velocities $v^{\pm}_{\eta,g} = u^{\pm}_{\eta,z} - (-1)^\eta \mathrm{sgn}(\mathcal{E}) v^{\pm}_{\eta,z}$ around two paired WNs at $\boldsymbol{k}^{\pm}_\eta$, where the density of states is $\rho_\eta = (2\pi^2 l_{\mathcal{E}}^2 \hbar |v^{\pm}_{\eta,g}|)^{-1}$ (with the Landau degeneracy included). We also introduce the AC phase into the magnon Hamiltonian Eq. (A1) through the Peierls substitution [43] and calculate its spectrum for an infinite long bar along the z direction with periodic boundary conditions in the x and y directions. For the electric field gradient $\mathcal{E} = 1/150\sqrt{3}$ in units of $\hbar c^2/g\mu_B$, the MLLs for the same model parameters as those in Figs. 3(a) and 3(b) are shown in Figs. 4(a) and 4(b), where the zeroth MLLs are the red curves. The MLLs for type-II WMs are shown in Appendix E.

V. MAGNONIC CHIRAL ANOMALY

To realize the MCA, one needs to drive WMs to flow from one WN to the other through the zeroth MLL. Due to the Zeeman energy $-\boldsymbol{B}\cdot\boldsymbol{\mu}$, an inhomogeneous magnetic field $\boldsymbol{B}$ can exert a driving force on magnons as $\hbar d\boldsymbol{k}/dt = \nabla(\boldsymbol{\mu}\cdot\boldsymbol{B})$ and results in the displacement of the lattice momentum

$$\delta\boldsymbol{k} = \frac{\nabla(\boldsymbol{\mu}\cdot\boldsymbol{B})\tau_m}{\hbar}, \tag{4}$$

where τ_m is magnon mean free time that is shorter than the period of Bloch oscillation due to all kinds of scattering as well as the intrinsic nonlinear effects for magnons, so that the transport of WMs through the zeroth MLL results in the nonconservation of chirality, the fingerprint of chiral anomaly [44]. To substantiate this claim, let us use the experimental magnon mean free time $\tau_m = 10^{-7} \sim 10^{-6}$ s of the ferromagnet yttrium iron garnet at 1.6 K [45] to estimate

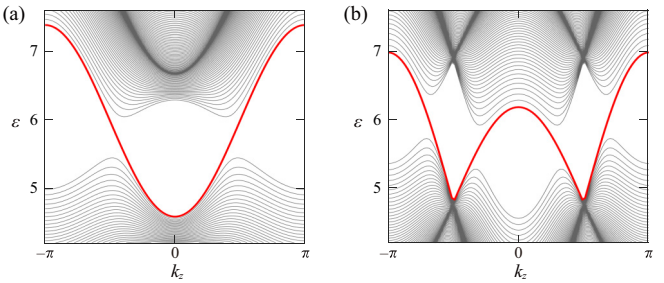

FIG. 4. (a) and (b) MLLs under an electric field gradient $\mathcal{E} = 1/150\sqrt{3}$ (in units of $\hbar c^2/g\mu_B$) for the model parameters identical to those in Figs. 3(a) and 3(b), respectively. The red curves are the zeroth MLLs.

TABLE I. Driving forces and pumping rates in the chiral anomaly of Weyl magnons and Weyl electrons. Here V is the sample volume; n_B and n_F are respectively the Bose-Einstein and Fermi-Dirac distributions; and ε is the energy of WNs (as well as the Fermi energy for Weyl electrons).

Weyl particle	Driving force	Pumping rate
Weyl magnon	$\frac{\hbar d\boldsymbol{k}}{dt} = \nabla(\boldsymbol{\mu}\cdot\boldsymbol{B})$	$\frac{dN}{dt} = \frac{Vn_B(\varepsilon)}{4\pi^2\hbar^2c^2}\nabla(\boldsymbol{\mu}\cdot\boldsymbol{B})\cdot[\nabla\times(\boldsymbol{E}\times\boldsymbol{\mu})]$
Weyl electron	$\frac{\hbar d\boldsymbol{k}}{dt} = -e\boldsymbol{E}$	$\frac{dN}{dt} = \frac{Ve^3n_F(\varepsilon)}{4\pi^2\hbar^2c}\boldsymbol{E}\cdot\boldsymbol{B}$

the necessary condition for observing the Bloch oscillation. The period of Bloch oscillation is $\tau_B = 2\pi\hbar/a\nabla(\boldsymbol{\mu}\cdot\boldsymbol{B}) = h/ag\mu_B\partial_z B \sim 0.36\,\mathrm{s\,T\,m^{-1}}/\partial_z B$, where the lattice constant $a \sim 1$ Å. Therefore the necessary condition for observing the Bloch oscillation is $\tau_B < \tau_m$, which yields $\partial_z B > 3.6\times 10^5\ \mathrm{T\,m^{-1}}$, too large to realize for natural crystals. The comparison of the driving forces and pumping rates for WMs and for Weyl electrons are summarized in Table I. In contrast to the electronic chiral anomaly in Weyl semimetals where parallel electric and magnetic fields are required, mutually perpendicular inhomogeneous electric and magnetic fields are needed for the MCA. Moreover, the electric and magnetic fields exchange their roles for WMs since the electric field generates MLLs while the magnetic field exerts driving forces, opposite roles in the chiral anomaly of Weyl electrons.

To detect the MCA, we consider a two-terminal device sketched in Fig. 5(a) under an inhomogeneous magnetic field along the z direction. Here a quasi-one-dimensional magnon conductor described by Eq. (1) and in the inhomogeneous electric field specified above is connected to two magnon reservoirs. Higher magnetic fields B_1 and B_2 are applied to the reservoirs to shift the magnon band bottoms to $\varepsilon_\eta - g\mu_B\Delta B/2$ and $\varepsilon_\eta + g\mu_B\Delta B/2$ (where $\Delta B = B_2 - B_1$) so that the system is at nonequilibrium as shown in Fig. 5(b). The imbalance of magnon concentrations between the two reservoirs within the energy window $[\varepsilon_\eta - g\mu_B\Delta B/2, \varepsilon_\eta + g\mu_B\Delta B/2]$ drives magnons to flow from the left to the right through the magnon conductor. In the ballistic regime where the sample length is smaller than the magnon mean free path, and for type-I WMs with only one pair of WNs at $\boldsymbol{k}_\eta^{\pm}$ ($\eta = 1$ or 2), the spin and heat currents (carried by magnons) through the zeroth MLL can be calculated from the Landauer-Büttiker theory [42] as

$$I_{s,\eta} = \int_{\varepsilon_\eta - g\mu_B\Delta B/2}^{\varepsilon_\eta + g\mu_B\Delta B/2} \frac{\hbar L_x L_y n_B(\varepsilon)d\varepsilon}{4\pi^2 l_{\mathcal{E}}^2\hbar} = G_{s,\eta}\Delta B,$$
$$I_{h,\eta} = \int_{\varepsilon_\eta - g\mu_B\Delta B/2}^{\varepsilon_\eta + g\mu_B\Delta B/2} \frac{\varepsilon L_x L_y n_B(\varepsilon)d\varepsilon}{4\pi^2 l_{\mathcal{E}}^2\hbar} = G_{h,\eta}\Delta B, \qquad (5)$$
$$G_{s,\eta} = \frac{L_x L_y g\mu_B n_B(\varepsilon_\eta)}{4\pi^2 l_{\mathcal{E}}^2},\ G_{h,\eta} = \frac{L_x L_y g\mu_B \varepsilon_\eta n_B(\varepsilon_\eta)}{4\pi^2 l_{\mathcal{E}}^2\hbar},$$

where $n_B(\varepsilon) = (e^{\varepsilon/k_BT} - 1)^{-1}$ is the Bose-Einstein distribution, $G_{s,\eta}$ and $G_{h,\eta}$ are respectively the spin and heat conductance (from the pair of WNs labeled by η) in the linear transport region. The contributions from higher MLLs ($n \geqslant 1$) are negligible when $g\mu_B\Delta B \ll 2\hbar\sqrt{\lambda_\eta}$ so that the energy window is within the energy gap between the first MLLs $\varepsilon_{\eta,1}^{\pm}(q_z)$, as shown in Fig. 5(b). Apparently, the spin (heat) conductance is linear in the electric field gradient as $G_{s(h),\eta} \propto l_{\mathcal{E}}^{-2} \propto |\mathcal{E}|$ due to the MLL degeneracy. Therefore, the MCA results in the positive and linear spin (heat) conductance, namely, the negative spin (heat) resistance as $R_{s(h),\eta} \propto |\mathcal{E}|^{-1}$. Because the ballistic magnon transport can be realized [46], these results are experimentally detectable and can serve as the signatures of the MCA.

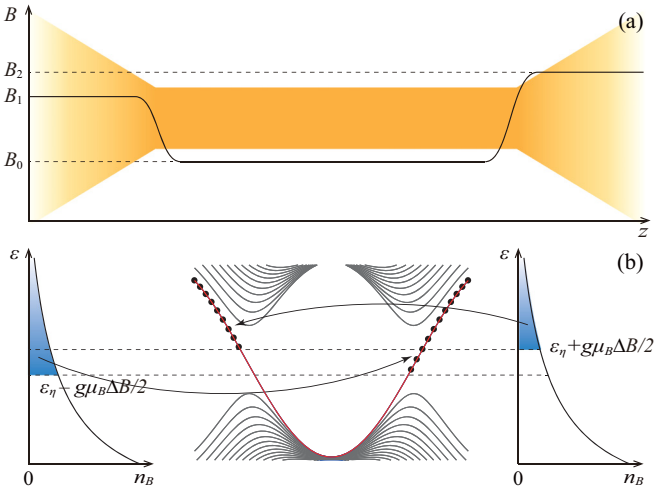

FIG. 5. (a) Schematic diagram of a two-terminal device under an inhomogeneous magnetic field along the z direction, in which the middle quasi-one-dimensional magnon conductor is connected to two magnon reservoirs. (b) Sketch of MLLs of the middle magnon conductor and magnon distribution functions of the left and right magnon reservoirs. The arrows indicate the injection of magnons from the reservoirs to the zeroth MLL (the red curve) of the middle magnon conductor.

VI. DISCUSSION

Before concluding this paper, we would like to make the following remarks.

(i) The transport results are valid for any number of pairs of WNs as long as WMs are type-I because the contributions of zeroth MLLs from different pairs of WNs are additive. Thus, the total spin (heat) conductance is simply $G_{s(h)} \simeq \sum_\eta G_{s(h),\eta}$, due to different pairs of WNs labeled by η. Transport of type-II WMs can be complicated because magnons can also be transported through the higher MLLs so that one

cannot distinguish the zeroth MLL from higher ones (see Appendix E).

(ii) The linear spin and heat conductance from the MCA indicates that electric field gradient can be used to control magnon transport. In the diffusive regime where the sample length is much larger than the magnon mean free path, the electric field dependence of spin and heat conductance should be sensitive to the detailed scattering processes. In fact, it was recently shown that the linear magnetoconductance can exist in disordered Weyl semimetals [47]. How it works for WMs is an open question.

(iii) Besides the transport measurement, one can also study the WMs by examining WNs and magnon arcs detectable by inelastic neutron scattering that was successfully used to probe the magnon bands of a topological magnon insulator [12].

(iv) There is a clear difference between the MCA and the electronic chiral anomaly. Instead of the parallel electric and magnetic fields used in the electronic chiral anomaly, the inhomogeneous electric and magnetic fields in the MCA are perpendicular to each other.

VII. CONCLUSION

In conclusion, stacked honeycomb ferromagnets can be both type-I and type-II WMs. Magnonic states can be quantized into MLLs in a proper inhomogeneous electric field through the AC effect. The MCA results in the linear dependence of spin and heat conductance on the electric field gradient when mutually perpendicular inhomogeneous electric and magnetic fields are applied. Our results provide new avenues to probe WMs and to control magnon transport by electric fields.

ACKNOWLEDGMENTS

This work is supported by the National Natural Science Foundation of China under Grant No. 11374249 and the Hong Kong Research Grants Council under Grants No. 16300117 and No. 16301816.

APPENDIX A: MAGNON HAMILTONIAN

According to the Holstein-Primakoff transformation [36], the spin operators are related to the magnon operators as $S^+_{i,l} = \sqrt{2S - n_{i,l}}\,c_{i,l}$ and $S^-_{i,l} = c^\dagger_{i,l}\sqrt{2S - n_{i,l}}$, where $n_{i,l} = c^\dagger_{i,l}c_{i,l}$, $S^\pm_{i,l} = S^x_{i,l} \pm i S^y_{i,l}$, and $c^\dagger_{i,l}$ and $c_{i,l}$ are magnon creation and annihilation operators satisfying the boson commutation relations. Substituting the transformation to Eq. (1), the spin Hamiltonian is transformed to a magnon Hamiltonian,

$$H = -JS\sum_{\langle i,j\rangle,l}(c^\dagger_{i,l}c_{j,l} + \text{H.c.}) - DS\sum_{\langle\langle i,j\rangle\rangle,l}(i\nu_{ij}c^\dagger_{i,l}c_{j,l} + \text{H.c.}) + \sum_{i,l}V_i c^\dagger_{i,l}c_{i,l} - \sum_{i,\langle l,l'\rangle}J_i S(c^\dagger_{i,l}c_{i,l'} + \text{H.c.}), \tag{A1}$$

where $V_i = 3JS + 2K_iS + 2J_iS$ is the sublattice-dependent on-site energy and high-order magnon-magnon interaction terms are neglected. Under the Fourier transformation $a_{\boldsymbol{k}} = \sqrt{2/N}\sum_{i\in\text{A},l} e^{i\boldsymbol{k}\cdot\boldsymbol{r}_{i,l}}c_{i,l}$ and $b_{\boldsymbol{k}} = \sqrt{2/N}\sum_{i\in\text{B},l} e^{i\boldsymbol{k}\cdot\boldsymbol{r}_{i,l}}c_{i,l}$, where $i \in$ A (B) for lattice sites on sublattice A (B) and N is the total number of lattice sites, the magnon Hamiltonian Eq. (A1) is block diagonalized in momentum space as $H = \sum_{\boldsymbol{k}} c^\dagger_{\boldsymbol{k}}\mathcal{H}(\boldsymbol{k})c_{\boldsymbol{k}}$, where $c_{\boldsymbol{k}} = (a_{\boldsymbol{k}}, b_{\boldsymbol{k}})^{\text{T}}$ and

$$\mathcal{H}(\boldsymbol{k}) = \varepsilon_0(\boldsymbol{k})I + \sum_{\beta=x,y,z} h_\beta(\boldsymbol{k})\sigma_\beta. \tag{A2}$$

The various terms here are $\varepsilon_0(\boldsymbol{k}) = 3JS + K_+S + J_+S(1-\cos k_z)$, $h_x(\boldsymbol{k}) = -JS\sum_{\alpha=1}^3\cos(\boldsymbol{k}\cdot\boldsymbol{a}_\alpha)$, $h_y(\boldsymbol{k}) = -JS\sum_{\alpha=1}^3\sin(\boldsymbol{k}\cdot\boldsymbol{a}_\alpha)$, and $h_z(\boldsymbol{k}) = 2DS\sum_{\alpha=1}^3\sin(\boldsymbol{k}\cdot\boldsymbol{b}_\alpha) + K_-S + J_-S(1-\cos k_z)$. Generally speaking, a system with both time-reversal ($\mathcal{T}$) and inversion ($\mathcal{P}$) symmetries can be a Dirac semimetal instead of a Weyl semimetal because $\mathcal{TP}$ imposes a double degeneracy on energy bands and the nontrivial band crossing involves four energy bands. There is no Kramer degeneracy for a magnetic system due to the intrinsic violation of time-reversal symmetry for magnetic order as well as $\mathcal{T}^2 = 1$ for spin-1 magnons [19]. Thus topological magnetic semimetals are in general Weyl semimetals. The inversion symmetry in the current model is also broken because of the anisotropic interlayer exchange interaction ($J_- \neq 0$) and anisotropy ($K_- \neq 0$) for the two sublattices so that $\mathcal{P}\mathcal{H}(\boldsymbol{k})\mathcal{P}^{-1} \neq \mathcal{H}(-\boldsymbol{k})$, where $\mathcal{P} = \sigma_x$ is the irreducible representation of the inversion operator.

The two energy bands $\varepsilon_\pm(\boldsymbol{k}) = \varepsilon_0(\boldsymbol{k}) \pm \sqrt{\sum_\beta h^2_\beta(\boldsymbol{k})}$ given by Eq. (A2) cross each other only when $h_{x(y,z)}(\boldsymbol{k}) = 0$. This can happen on HKH and H′K′H′ of the first bulk BZ because $h_{x(y)}(\boldsymbol{k}) = 0$ and $h_z(\boldsymbol{k}) = \pm 3\sqrt{3}DS + K_-S + J_-S(1-\cos k_z)$ for $\boldsymbol{k} = (\pm 4\pi/3\sqrt{3}, 0, k_z)$. Therefore WNs are located at $\boldsymbol{k}^\pm_1 = (-4\pi/3\sqrt{3}, 0, \pm\cos^{-1} f_1)$ and $\boldsymbol{k}^\pm_2 = (4\pi/3\sqrt{3}, 0, \pm\cos^{-1} f_2)$, with $f_\eta = K_-/J_- + 1 + (-1)^\eta 3\sqrt{3}D/J_-$ for $\eta = 1$ or 2. Conditions of $|f_\eta| \leqslant 1$ result in the WM phases and four phase boundaries of $K_- = \pm 3\sqrt{3}D$ (solid lines) and $K_- + 2J_- = \pm 3\sqrt{3}D$ (dashed lines) in Fig. 2. Otherwise the two magnon bands are gapped.

APPENDIX B: DIPOLE-DIPOLE INTERACTION

The NN intralayer and interlayer magnetic dipole-dipole interactions (DDIs) in stacked honeycomb ferromagnets are

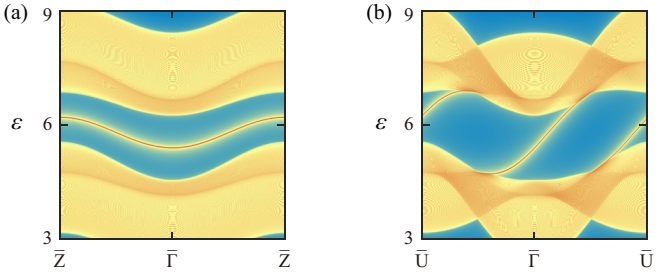

FIG. 6. Density plots of the front (100) surface spectral function along $\bar{\text{Z}}\bar{\Gamma}\bar{\text{Z}}$ and $\bar{\text{U}}\bar{\Gamma}\bar{\text{U}}$ for the topological magnon insulator whose model parameters are specified in Appendix D.

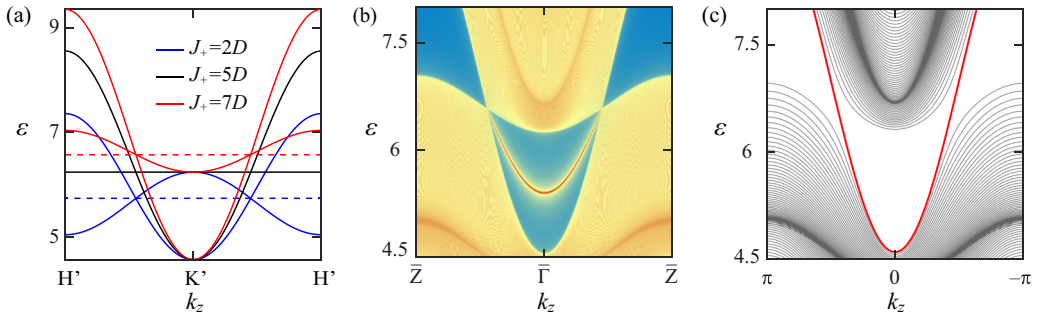

FIG. 7. (a) Energy bands along H′K′H′ for WMs with $J_+ = 2D, 5D$, and $7D$, while the other model parameters are specified in Appendix E. (b) Density plot of the front (100) surface spectral function for the type-II WM with $J_+ = 7D$ in panel (a) and along $\bar{Z}\bar{\Gamma}\bar{Z}$. (c) MLLs of the type-II WM under an inhomogeneous electric field specified in Appendix E. The red curve is the zeroth MLL.

described by the following Hamiltonians:

$$H_D^{\text{intra}} = \sum_{\langle i,j\rangle,l} \frac{g^2\mu_B^2}{r_{ij}^3}\left(\boldsymbol{S}_{i,l}\cdot\boldsymbol{S}_{j,l} - \frac{3(\boldsymbol{S}_{i,l}\cdot\boldsymbol{r}_{ij})(\boldsymbol{S}_{j,l}\cdot\boldsymbol{r}_{ij})}{r_{ij}^2}\right),$$

$$H_D^{\text{inter}} = \sum_{i,\langle l,l'\rangle} \frac{g^2\mu_B^2}{d_{ll'}^3}\left(\boldsymbol{S}_{i,l}\cdot\boldsymbol{S}_{i,l'} - \frac{3(\boldsymbol{S}_{i,l}\cdot\boldsymbol{d}_{ll'})(\boldsymbol{S}_{i,l'}\cdot\boldsymbol{d}_{ll'})}{d_{ll'}^2}\right), \tag{B1}$$

where $\boldsymbol{r}_{ij}$ and $\boldsymbol{d}_{ll'}$ are vectors connecting the NN intralayer and interlayer lattice sites [48], respectively, so that $r_{ij} = d_{ll'} = 1$. Under the Holstein-Primakoff transformation and the Fourier transformation, the total Hamiltonian (with DDIs but without magnon-magnon interactions) is

$$\widetilde{H} = H + H_D^{\text{intra}} + H_D^{\text{inter}} = \sum_{\boldsymbol{k}} \Psi_{\boldsymbol{k}}^\dagger \widetilde{\mathcal{H}}(\boldsymbol{k})\Psi_{\boldsymbol{k}}, \tag{B2}$$

where $\Psi_{\boldsymbol{k}} = (a_{\boldsymbol{k}}, b_{\boldsymbol{k}}, a_{-\boldsymbol{k}}^\dagger, b_{-\boldsymbol{k}}^\dagger)^{\mathrm{T}}$ is the Nambu basis and

$$\widetilde{\mathcal{H}}(\boldsymbol{k}) = \begin{pmatrix} \widetilde{\varepsilon}_0(\boldsymbol{k}) + \widetilde{h}_z(\boldsymbol{k}) & \widetilde{h}_x(\boldsymbol{k}) - i\widetilde{h}_y(\boldsymbol{k}) & 0 & \widetilde{f}(\boldsymbol{k}) \\ \widetilde{h}_x(\boldsymbol{k}) + i\widetilde{h}_y(\boldsymbol{k}) & \widetilde{\varepsilon}_0(\boldsymbol{k}) - \widetilde{h}_z(\boldsymbol{k}) & \widetilde{f}(-\boldsymbol{k}) & 0 \\ 0 & \widetilde{f}^*(-\boldsymbol{k}) & \widetilde{\varepsilon}_0(-\boldsymbol{k}) + \widetilde{h}_z(-\boldsymbol{k}) & \widetilde{h}_x(-\boldsymbol{k}) + i\widetilde{h}_y(-\boldsymbol{k}) \\ \widetilde{f}^*(\boldsymbol{k}) & 0 & \widetilde{h}_x(-\boldsymbol{k}) - i\widetilde{h}_y(-\boldsymbol{k}) & \widetilde{\varepsilon}_0(-\boldsymbol{k}) - \widetilde{h}_z(-\boldsymbol{k}) \end{pmatrix}. \tag{B3}$$

The various terms in Eq. (B3) are $\widetilde{\varepsilon}_0(\boldsymbol{k}) = \varepsilon_0(\boldsymbol{k})/2 + g^2\mu_B^2 S(1+2\cos k_z)/2$, $\widetilde{h}_x(\boldsymbol{k}) = h_x(\boldsymbol{k})/2 - g^2\mu_B^2 S\sum_{\alpha=1}^3 \cos(\boldsymbol{k}\cdot\boldsymbol{a}_\alpha)/4$, $\widetilde{h}_y(\boldsymbol{k}) = h_y(\boldsymbol{k})/2 - g^2\mu_B^2 S\sum_{\alpha=1}^3 \sin(\boldsymbol{k}\cdot\boldsymbol{a}_\alpha)/4$, $\widetilde{h}_z(\boldsymbol{k}) = h_z(\boldsymbol{k})/2$, and $\widetilde{f}(\boldsymbol{k}) = -3g^2\mu_B^2 S\sum_{\alpha=1}^3 e^{i2\theta_\alpha}e^{-i\boldsymbol{k}\cdot\boldsymbol{a}_\alpha}/4$, where $\theta_1 = 3\pi/2$, $\theta_2 = \pi/6$, and $\theta_3 = 5\pi/6$. Now we focus on $\boldsymbol{k} = (\pm 4\pi/3\sqrt{3}, 0, k_z)$ on HKH and H′K′H′, where WNs exist in the absence of DDIs. The four eigenvalues given by Eq. (B3) are

$$\begin{aligned}
\widetilde{\varepsilon}_1(\boldsymbol{k}) &= \widetilde{\varepsilon}_0(\boldsymbol{k}) + \frac{3\sqrt{3}DS}{2} + \frac{|K_-S + J_-S(1-\cos k_z)|}{2}, \\
\widetilde{\varepsilon}_2(\boldsymbol{k}) &= \widetilde{\varepsilon}_0(\boldsymbol{k}) + \frac{3\sqrt{3}DS}{2} - \frac{|K_-S + J_-S(1-\cos k_z)|}{2}, \\
\widetilde{\varepsilon}_3(\boldsymbol{k}) &= \widetilde{\varepsilon}_0(\boldsymbol{k}) - \frac{3\sqrt{3}DS}{2} + \frac{\sqrt{81g^4\mu_B^4S^2/4 + [K_-S + J_-S(1-\cos k_z)]^2}}{2}, \\
\widetilde{\varepsilon}_4(\boldsymbol{k}) &= \widetilde{\varepsilon}_0(\boldsymbol{k}) - \frac{3\sqrt{3}DS}{2} - \frac{\sqrt{81g^4\mu_B^4S^2/4 + [K_-S + J_-S(1-\cos k_z)]^2}}{2}.
\end{aligned} \tag{B4}$$

Apparently, $\widetilde{\varepsilon}_1(\boldsymbol{k})$ and $\widetilde{\varepsilon}_2(\boldsymbol{k})$ can cross each other when

$$K_-S + J_-S(1-\cos k_z) = 0. \tag{B5}$$

However, $\widetilde{\varepsilon}_3(\boldsymbol{k})$ and $\widetilde{\varepsilon}_4(\boldsymbol{k})$ are gapped for nonvanishing DDI. Moreover $\widetilde{\varepsilon}_2(\boldsymbol{k})$ and $\widetilde{\varepsilon}_3(\boldsymbol{k})$ can cross each other when

$$3\sqrt{3}DS - \frac{|K_-S + J_-S(1-\cos k_z)|}{2} - \frac{\sqrt{81g^4\mu_B^4S^2/4 + [K_-S + J_-S(1-\cos k_z)]^2}}{2} = 0, \tag{B6}$$

and if DDIs vanish, this condition just recovers the phase diagram (Fig. 2). Therefore, we can conclude that our main results survive in the presence of DDIs but the phase diagram and positions of WNs are modified as expected. Because the

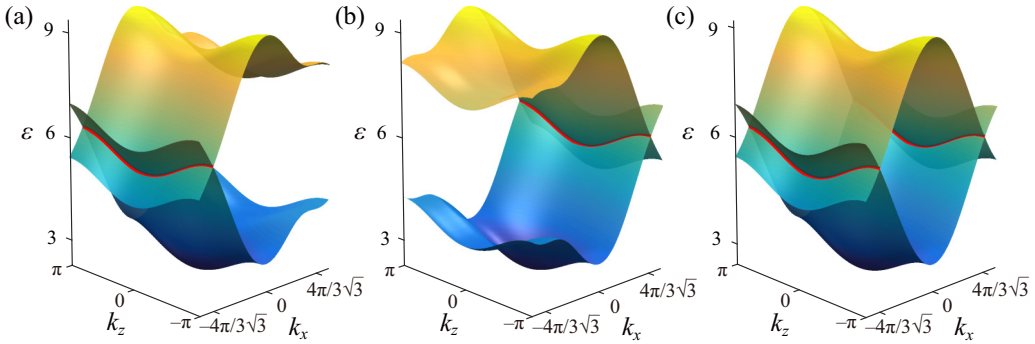

FIG. 8. (a)–(c) Energy bands for nodal-line magnons specified in Appendix F. Nodal lines are marked by the red curves.

DDI is usually much weaker than the other interactions studied in the Hamiltonian Eq. (1), it is reasonable to omit the DDI. It has been shown that theoretical models without DDIs can well describe the experimental results [3,12].

APPENDIX C: CHERN NUMBER

One can view the three-dimensional system as coupled multiple two-dimensional subsystems: $\mathcal{H}(\boldsymbol{k}) = \sum_{k_z} \mathcal{H}_{k_z}(k_x,k_y)$, where k_z is the subsystem index. In order to elaborate the existence of topologically protected surface states in both WM and topological magnon insulator phases, we calculate the Chern number of the subsystem described by $\mathcal{H}_{k_z}(k_x,k_y)$ for fixed k_z. The Chern number as a function of k_z is

$$C(k_z) = \sum_{\eta=1,2} \frac{(-1)^\eta}{2} \mathrm{sgn}[(-1)^\eta 3\sqrt{3}D + K_- + J_-(1-\cos k_z)]. \quad \text{(C1)}$$

In the WM phases, the Chern number changes from 0 to ± 1 or vice versa when the constant k_z plane passes through a WN in momentum space. Therefore, the topologically protected surface states exist between WNs as shown in Figs. 3(e) and 3(f). In the topological magnon insulator phase, $C(k_z) = \pm 1$ for all k_z and topologically protected surface states exist in the magnon bulk band gap (see Appendix D). In the trivial phase, $C(k_z) = 0$ for all k_z.

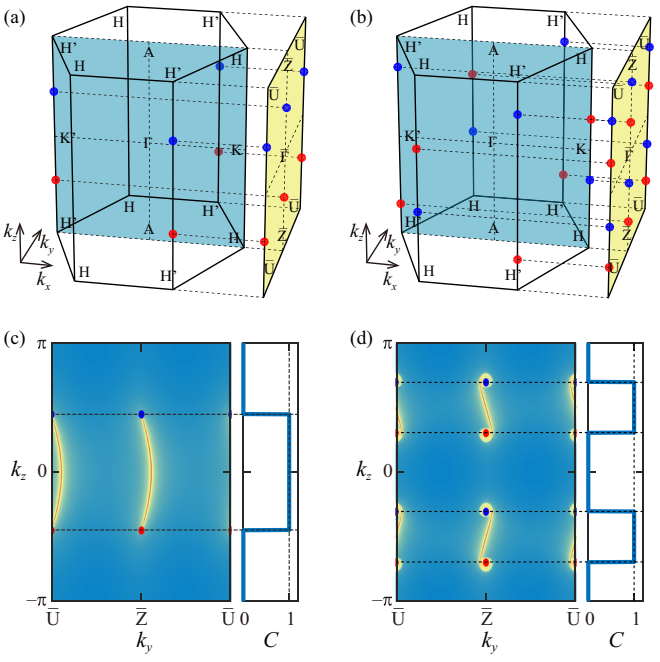

FIG. 9. (a) and (b) Positions of WNs in Figs. 3(a) and 3(b) are schematically indicated by the red and blue dots (for chirality ± 1) in the first bulk BZ and the first (100) surface BZ. (c) and (d) Density plots of the corresponding front (100) surface spectral functions in the first (100) surface BZ are shown in the left panels. The red curves connecting WNs are magnon arcs. The corresponding Chen numbers $C(k_z)$ are shown in the right panels.

APPENDIX D: TOPOLOGICAL MAGNON INSULATOR

To visualize the topologically protected surface states of topological magnon insulators, we compute the front (100) surface spectral function for model parameters $D = 0.2J$, $K_+ = 12D$, $J_+ = 2D$, and $(K_-,J_-) = (D,0.5D)$ in the topological magnon insulator phase (the green region in Fig. 2) with $C(k_z) = 1$ for all k_z. The density plot of the front (100) surface spectral function along $\bar{Z}\bar{\Gamma}\bar{Z}$ and $\bar{U}\bar{\Gamma}\bar{U}$ of the first (100) surface BZ are respectively shown in Figs. 6(a) and 6(b). As expected, the bulk states are gapped and topologically protected surface states exist in the bulk band gap.

APPENDIX E: TYPE-II WEYL MAGNON

In the effective Weyl Hamiltonian Eq. (2), the third term gives a Weyl cone while the second term tilts the Weyl cone along the k_z direction in momentum space. According to the criteria of the type-II Weyl semimetal in Ref. [41], we obtain the condition for WMs becoming type-II in our model as $|u^{\pm}_{\eta,z}| > |v^{\pm}_{\eta,z}| \Rightarrow |J_+| > |J_-|$. To confirm this result, we compute the magnon bands for the model parameters $D = 0.2J$, $K_+ = 12D$, $(K_-,J_-) = (D,5D)$, and $J_+ = \{2D,5D,7D\}$. In the current case, there is a pair of WNs located on H′K′H′ of the first bulk BZ. Therefore, we plot the magnon bands along H′K′H′ and the results are shown in Fig. 7(a). Indeed, the system changes from the type-I WM to the type-II WM at $J_+ = 5D = J_-$ where one magnon band is flat along H′K′H′. For $J_+ = 7D > J_-$, it is clearly shown that the Weyl cones are tilted to be type-II.

Because the tilt of the Weyl cone does not change its band topology, topologically protected surface states also exist between WNs in type-II WMs. In Fig. 7(b), we show the front (100) surface spectral function of the type-II WM with $J_+ = 7D$ in Fig. 7(a) along $\bar{Z}\bar{\Gamma}\bar{Z}$ of the first (100) surface BZ. Apparently, the type-II WNs and surface states are identified. Under the inhomogeneous electric field $\boldsymbol{E} = (\mathcal{E}x,0,0)$, with $\mathcal{E} = 1/100\sqrt{3}$ in units of $\hbar c^2/g\mu_B$, MLLs of the type-II WM are shown in Fig. 7(c). The zeroth MLL (marked by the red curve) is still chiral but cannot be separated from higher MLLs, because there is no band gap between the first MLLs.

APPENDIX F: NODAL-LINE MAGNON

At the phase boundary crossing points $(K_-/D, J_-/D) = (\pm 3\sqrt{3},0)$ and for $\boldsymbol{k} = (\mp 4\pi/3\sqrt{3},0,k_z)$, $h_{x(y,z)}(\boldsymbol{k}) = 0$ for all k_z. Namely, two bands cross on nodal lines of H′K′H′ and HKH, respectively, so that the system becomes nodal-line magnons. In order to visualize these nodal lines, we compute the energy bands for the system at two phase boundary crossing points as shown in Figs. 8(a) and 8(b), while the other model parameters $D = 0.2J$, $K_+ = 12D$, and $J_+ = 2D$ are fixed. The nodal lines are marked by red curves. When $K_- = D = 0$ (with the other parameters unchanged), the two points merge together and the two nodal lines coexist as shown in Fig. 8(c).

APPENDIX G: MAGNON ARC

For the energy bands in Figs. 3(a) and 3(b), WNs of chirality ± 1 in the first bulk BZ and their projection in the first (100) surface BZ are respectively denoted by the red and blue dots in Figs. 9(a) and 9(b). In order to visualize the magnon arcs formed by topologically protected surface states near the WN energy on sample surfaces, we compute the corresponding front (100) surface spectral functions within the first (100) surface BZ for the energies $\varepsilon = \varepsilon_1$ [for Fig. 9(a)] and $(\varepsilon_1 + \varepsilon_2)/2$ [for Fig. 9(b)], as shown in the left panels of Figs. 9(c) and 9(d). Apparently, the surface states with high density (red color) on sample surfaces form magnon arcs that connect WNs of opposite chirality. The corresponding Chern numbers $C(k_z)$ are computed according to Eq. (C1) and shown in the right panels of Figs. 9(c) and 9(d). Indeed, the magnon arcs accompany nonzero Chern numbers as expected.

[1] S. Fujimoto, Phys. Rev. Lett. **103**, 047203 (2009).
[2] H. Katsura, N. Nagaosa, and P. A. Lee, Phys. Rev. Lett. **104**, 066403 (2010).
[3] Y. Onose, T. Ideue, H. Katsura, Y. Shiomi, N. Nagaosa, and Y. Tokura, Science **329**, 297 (2010).
[4] R. Matsumoto and S. Murakami, Phys. Rev. Lett. **106**, 197202 (2011); R. Matsumoto, R. Shindou, and S. Murakami, Phys. Rev. B **89**, 054420 (2014).
[5] L. Zhang, J. Ren, J.-S. Wang, and B. Li, Phys. Rev. B **87**, 144101 (2013).
[6] R. Shindou, J. I. Ohe, R. Matsumoto, S. Murakami, and E. Saitoh, Phys. Rev. B **87**, 174402 (2013); R. Shindou, R. Matsumoto, S. Murakami, and J. I. Ohe, *ibid.* **87**, 174427 (2013).
[7] M. Mochizuki, X. Z. Yu, S. Seki, N. Kanazawa, W. Koshibae, J. Zang, M. Mostovoy, Y. Tokura, and N. Nagaosa, Nat. Mater. **13**, 241 (2014).
[8] A. Mook, J. Henk, and I. Mertig, Phys. Rev. B **90**, 024412 (2014).
[9] M. Mena, R. S. Perry, T. G. Perring, M. D. Le, S. Guerrero, M. Storni, D. T. Adroja, Ch. Rüegg, and D. F. McMorrow, Phys. Rev. Lett. **113**, 047202 (2014).
[10] I. Lisenkov, V. Tyberkevych, A. Slavin, P. Bondarenko, B. A. Ivanov, E. Bankowski, T. Meitzler, and S. Nikitov, Phys. Rev. B **90**, 104417 (2014).
[11] H. Lee, J. H. Han, and P. A. Lee, Phys. Rev. B **91**, 125413 (2015).
[12] R. Chisnell, J. S. Helton, D. E. Freedman, D. K. Singh, R. I. Bewley, D. G. Nocera, and Y. S. Lee, Phys. Rev. Lett. **115**, 147201 (2015).
[13] C.-E. Bardyn, T. Karzig, G. Refael, and T. C. H. Liew, Phys. Rev. B **93**, 020502(R) (2016).
[14] S. A. Owerre, J. Phys.: Condens. Matter **28**, 386001 (2016); Sci. Rep. **7**, 6931 (2017).
[15] R. Cheng, S. Okamoto, and D. Xiao, Phys. Rev. Lett. **117**, 217202 (2016).
[16] V. A. Zyuzin and A. A. Kovalev, Phys. Rev. Lett. **117**, 217203 (2016).
[17] S. K. Kim, H. Ochoa, R. Zarzuela, and Y. Tserkovnyak, Phys. Rev. Lett. **117**, 227201 (2016).
[18] J. Fransson, A. M. Black-Schaffer, and A. V. Balatsky, Phys. Rev. B **94**, 075401 (2016).
[19] F. Y. Li, Y. D. Li, Y. B. Kim, L. Balents, Y. Yu, and G. Chen, Nat. Commun. **7**, 12691 (2016).
[20] A. Mook, J. Henk, and I. Mertig, Phys. Rev. Lett. **117**, 157204 (2016).
[21] Y. Su, X. S. Wang, and X. R. Wang, Phys. Rev. B **95**, 224403 (2017).
[22] A. Mook, J. Henk, and I. Mertig, Phys. Rev. B. **95**, 014418 (2017).
[23] X. S. Wang, Y. Su, and X. R. Wang, Phys. Rev. B. **95**, 014435 (2017).
[24] S. O. Demokritov and A. N. Slavin, *Magnonics: From Fundamentals to Applications*, Topics in Applied Physics Vol. 125 (Springer, Berlin, 2013).
[25] D. Grundler, Nat. Phys. **11**, 438 (2015).
[26] B. Lenk, H. Ulrichs, F. Garbs, and M. Münzenberg, Phys. Rep. **507**, 107 (2011).
[27] A. V. Chumak, V. I. Vasyuchka, A. A. Serga, and B. Hillebrands, Nat. Phys. **11**, 453 (2015).
[28] Y. Kajiwara, K. Harii, S. Takahashi, J. Ohe, K. Uchida, M. Mizuguchi, H. Umezawa, K. Kawai, K. Ando, K. Takanashi, S. Maekawa, and E. Saitoh, Nature (London) **464**, 262 (2010).
[29] L. J. Cornelissen, J. Liu, R. A. Duine, J. B. Youssef, and B. J. van Wees, Nat. Phys. **11**, 1022 (2015).
[30] P. Yan, X. S. Wang, and X. R. Wang, Phys. Rev. Lett. **107**, 177207 (2011).

[31] X. S. Wang, P. Yan, Y. H. Shen, G. E. W. Bauer, and X. R. Wang, Phys. Rev. Lett. **109**, 167209 (2012).
[32] B. Hu and X. R. Wang, Phys. Rev. Lett. **111**, 027205 (2013).
[33] Y. Aharonov and A. Casher, Phys. Rev. Lett. **53**, 319 (1984).
[34] The various in-plane vectors in Fig. 1(a) are set as $\boldsymbol{a}_1 = (0,-1,0)$, $\boldsymbol{a}_2 = (\sqrt{3}/2,1/2,0)$, $\boldsymbol{a}_3 = (-\sqrt{3}/2,1/2,0)$, $\boldsymbol{b}_1 = (\sqrt{3}/2,-3/2,0)$, $\boldsymbol{b}_2 = (\sqrt{3}/2,3/2,0)$, and $\boldsymbol{b}_3 = (-\sqrt{3},0,0)$, where the distance between nearest-neighbor intralayer lattice sites is set as unity.
[35] I. Dzyaloshinskii, J. Phys. Chem. Solids **4**, 241 (1958); T. Moriya, Phys. Rev. **120**, 91 (1960).
[36] T. Holstein and H. Primakoff, Phys. Rev. **58**, 1098 (1940).
[37] P. Hosur and X. L. Qi, C. R. Phys. **14**, 857 (2013).
[38] H. B. Nielsen and M. Ninomiya, Phys. Lett. B **130**, 389 (1983).
[39] X. Wan, A. M. Turner, A. Vishwanath, and S. Y. Savrasov, Phys. Rev. B **83**, 205101 (2011).
[40] Y. Xu, F. Zhang, and C.-W. Zhang, Phys. Rev. Lett. **115**, 265304 (2015).
[41] A. A. Soluyanov, D. Gresch, Z. Wang, Q. Wu, M. Troyer, X. Dai, and B. A. Bernevig, Nature (London) **527**, 495 (2015).
[42] F. Meier and D. Loss, Phys. Rev. Lett. **90**, 167204 (2003); K. Nakata, J. Klinovaja, and D. Loss, Phys. Rev. B **95**, 125429 (2017).
[43] X. R. Wang, Phys. Rev. B **53**, 12035 (1996).
[44] A. Burkov, Science **350**, 378 (2015).
[45] R. L. Douglass, Phys. Rev. **129**, 1132 (1963).
[46] S. Y. Li, L. Taillefer, C. H. Wang, and X. H. Chen, Phys. Rev. Lett. **95**, 156603 (2005).
[47] H. Z. Lu and S. Q. Shen, Front. Phys. **12**, 127201 (2017).
[48] M. G. Cottam, J. Phys. C: Solid State Phys. **4**, 2658 (1971).